Liu *et al.*
Intelligent Marine Technology and Systems (2024) 2:30
https://doi.org/10.1007/s44295-024-00044-1

imts Intelligent Marine Technology and Systems

REVIEW Open Access

Calculation algorithm for spectral irradiance using broad-band optical filter data

Yilin Liu[1,2,3], Jinping Zhao[2,3*], Ping Chen[4], Xianyao Chen[1], Li Yi[2], Xiaoyu Wang[1] and Tao Li[2]

Abstract

A disposable miniature radiometer has been developed using optical filters for spectral separation. Limitations in accurately retrieving irradiance from the broad-band measurement results can be attributed to the broad-band filters. This paper proposes an algorithm for spectral irradiance using broad-band optical filter data (SIBOF algorithm) to achieve precise retrieved irradiance through four correction steps. First, the algorithm uses an energy ratio method to adjust the broad-band data to narrow-band data. The energy ratio is derived from the reference lamp spectrum and measured optical filter transmissivities. Second, the algorithm corrects for filter transmissivity differences by multiplying the normalized spectral transmissivities by calibration coefficients. The third step involves polarization correction, compensating for additional transmissivity caused by polarization effects from the film overlying on the cosine collector, thus eliminating errors due to film polarization. The fourth step involves radiative heating correction, where fitting curves and coefficients are used to analyze the relationship between irradiance deviation and actual irradiance to correct the data. Standardized tests indicate that, after applying the four corrections, the results are highly consistent with the irradiance from the reference radiometer, demonstrating that these correction steps constitute a reliable algorithm for spectral irradiance using broad-band optical filter data. In April 2024, a 20-day sea fog sounding observation was conducted at the Qianliyan Ocean Station. The irradiance data from the miniature radiometers before launch were corrected and compared with those measured by the reference radiometer on the ground. Results indicate that the irradiance retrieved through the algorithm was in good agreement with the measurements from the reference radiometer, validating its performance across various weather conditions.

Keywords Broad-band optical filter, Transmissivity correction, Polarization correction, Radiative heating correction, Irradiance retrieval, Broad-band radiometer

1 Introduction

Irradiance is a crucial optical parameter in various optical fields (Thuillier et al. 2022). In atmospheric science, irradiance is primarily used to quantify natural light radiation, which is measured in units of energy flux, W/m^2; meanwhile, spectral irradiance, which represents the energy flux per wavelength, is measured in mW/(m^2 nm) (Ermolli et al. 2013; Meftah et al. 2016).

Natural light, related to solar radiation, is generally categorized into direct light (includes forward-scattered light) and scattered light (Gray et al. 2010; Wang 2014). Direct light refers to the radiation flux of solar radiation that reaches the position of a radiometer after being attenuated by absorption and scattering of the substances in the atmosphere (Dunkelman and Scolnik 1959; Eltbaakh et al. 2012; Khalil and Shaffie 2016). By contrast, scattered light is solar radiation scattered by atmospheric molecules and suspended particles (Mueller 1938; Fan

*Correspondence:
Jinping Zhao
jpzhao@ouc.edu.cn
[1] Key Laboratory of Physical Oceanography, Ocean University of China, Qingdao 266100, China
[2] College of Oceanic and Atmospheric Sciences, Ocean University of China, Qingdao 266100, China
[3] Guanchao Marine Technology Co., Ltd., Qingdao 266011, China
[4] Institute of Oceanographic Instrumentation, Qilu University of Technology (Shandong Academy of Sciences), Qingdao 266100, China

et al. 2009; Hahn 2009). In the atmosphere, scattering by air molecules is known as Rayleigh scattering (McCartney 1976), which gives the sky its blue color on clear days (Young 1981; Bird and Riordan 1986; Kleinman and Senior 1986). Scattering by larger particles, such as fog droplets and aerosols, is referred to as Mie scattering (Wiscombe 1980; Zimmer et al. 2003; Ma 2007). In addition to scattering, the atmospheric substances can also absorb solar radiation and convert it into heat energy (Bird and Riordan 1986; Mercado et al. 2009), which is then transferred to the atmosphere in other forms.

In optical observation, the direction of incident light is crucial when measuring direct light. In practice, direct and scattered light is typically present (Bird and Riordan 1986; Gray et al. 2010). Despite the difficulty in determining the exact proportion of direct and scattered light for a general radiometer, the direction of light must be considered, especially when the radiometer moves in the sky, as will be introduced later.

A radiometer is an instrument used to measure irradiance by detecting the signal of optical radiation through the photoelectric effect and energy conservation principles. This technology is well-established, with various types of radiometers employed to measure multispectral or hyperspectral irradiance (Tatsiankou et al. 2016; Girish et al. 2020; Michael et al. 2020; Richard et al. 2020; Riihimaki et al. 2021). The main difference in irradiance measurement technology lies in spectral separation. Commonly, hyperspectral radiometers use grating-based separation (Li et al. 2022; Pagano et al. 2022; Zhang et al. 2024b), while radiometers designed for fewer spectral bands employ filter-based separation (Yang et al. 2021; Sun et al. 2022).

Ideal optical signals are characterized by rectangular bandpass signals; thus, they remain constant within a bandwidth of $\pm\Delta\lambda$ (unit: nm) and zero outside this range. The output signals of grating- and filter-based separation are essentially peaked, differing notably from rectangular (Yang et al. 2021; Zhang et al. 2024a, b). Accurate measurement of hyperspectral irradiance requires a narrow bandwidth to ensure precision (Luo et al. 2016). Grating-based separation instruments can achieve a bandwidth of ± 3 nm, whereas filters have notably wider bandwidths, with a full-width half maximum greater than ± 5 nm. The peaked structure of signals through filters and their broader bandwidth can lead to out-of-band light input (Du 2023), which is mistaken as 'signals', resulting in higher output voltage. This issue is one of the main sources of error (Okhonin et al. 2015), particularly for specific observation requirements, which will be discussed further in the next paragraph. Addressing this challenge remains an ongoing area of research.

A miniature radiometer (Patent No. 201910302823.2) that can be carried aloft by a sounding balloon has been developed to detect the downward irradiance profile of the atmosphere. Physical parameters and material distribution in the atmosphere can be derived from this data. This radiometer is called the fog visibility profiler (FVP). The FVP uses five monochromatic channels and one full-spectral channel, each equipped with an optical filter to provide band-pass signals. As a disposable instrument, the FVP cannot use high-precision but expensive components. Therefore, this instrument relies on broad-band filters while aiming to achieve measurement accuracy similar to that of narrow-band instruments. However, for this observation requirement, using data collected from broad-band filters to accurately determine spectral irradiance is difficult, with errors occasionally exceeding the actual values by more than double. Therefore, accurately measuring spectral irradiance using cost-effective broad-band filters remains a critical challenge.

This study explores the characteristics of the data measured by broad-band optical filters and identifies sources of errors. Section 2 introduces a four-step correction method for broad-band data, which comprehensively considers factors such as bandwidth and spectrum transmissivity of filters, polarization effects of the film overlying on the cosine collector, and solar radiative heating. Section 3 validates this correction algorithm, and Section 4 applies the algorithm to the broad-band data from in situ observation. The corrected results are highly consistent with the measurements from the reference narrow-band radiometer. This four-step algorithm is referred to as the algorithm for spectral irradiance using broad-band optical filter data (SIBOF algorithm). Finally, Section 5 presents the results and discussion.

2 Bandwidth correction algorithm for irradiance

The principle of a miniature radiometer relies on the photoelectric effect, using photodiodes as the data acquisition units. The photodiode captures the incident light that passes through an optical filter, generating an electric current. The current is then converted into an output voltage, which serves as the output signal. Figure 1 shows the optical signal acquisition system of a miniature radiometer meter, which comprises the following components: an optical filter (III) that captures light within a specific wavelength range (Epstein 1952; Luo et al. 2016); a cosine collector (II) made from Spectralon, also known as a Lambertian reflector, which converts light from all directions into cosine-scattered light (Bruegge et al. 1993; Murgai et al. 2020); a low-cost film (I) that secures the cosine collector and makes the optical acquisition system waterproof; a photodiode (V) and a circuit board (VI)

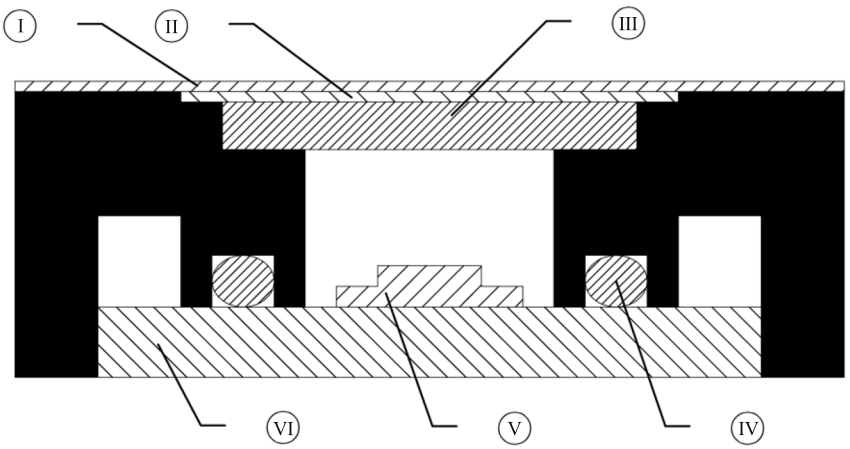

Fig. 1 Cross-sectional view of the components of the optical signal acquisition system in a multispectral radiometer. I: film, II: cosine collector, III: optical filter, IV: sealing ring, V: photodiode, and VI: data acquisition circuit board

that collect light signals; and a sealing ring (IV) that optically seals the entire optical signal acquisition system.

The optical signal acquisition system, which takes the filter as the main component, has a relatively broad bandwidth, leading to large errors during irradiance data acquisition. Sections 2.1 to 2.7 introduce the data correction methods to meet the needs of high-precision irradiance measurement.

2.1 Standard calibration method for radiometer

Herein, the variables used in this paper are introduced: λ represents the wavelength, λ_n represents the central wavelength of the n-th spectral band, and $\Delta\lambda$ represents the half bandwidth. The ideal narrow-band optical signal is a rectangular wave, which remains constant within the bandwidth $\pm\Delta\lambda$ (unit: nm) and zero outside the bandwidth. Suppose the measured input energy for a spectral band is $E(\lambda)$ (unit: mW/(m^2 nm)) and the output voltage is $v(\lambda)$ (unit: V). The relationship between the two is described using a linear function (Okhonin et al. 2015):

$$E(\lambda) = p(\lambda_n)v(\lambda) + q(\lambda_n), \tag{1}$$

where $p(\lambda_n)$ and $q(\lambda_n)$ are the slope and intercept of the linear fitting, respectively. In the absence of incident radiation, the output voltage due to dark current, $v_{\text{dark}}(\lambda_n)$, can be measured, changing Eq. (1) into the following:

$$E(\lambda_n) = \frac{v(\lambda_n) - v_{\text{dark}}(\lambda_n)}{S(\lambda_n)}, \tag{2}$$

where the calibration coefficient $S(\lambda_n)$ is obtained through optical calibration by measuring a reference lamp in a darkroom (Mueller and Fargion 2003):

$$S(\lambda_n) = \frac{v_{\text{sd}}(\lambda_n) - v_{\text{dark}}(\lambda_n)}{E_{\text{sd}}(\lambda_n)}, \tag{3}$$

where $E_{\text{sd}}(\lambda_n)$ is the irradiance of the reference lamp, and $v_{\text{sd}}(\lambda_n)$ is the output voltage when measuring the reference lamp with a diaphragm to remove stray light. Once $S(\lambda_n)$ is determined, the accurate spectral irradiance can be calculated using Eq. (2).

However, Eq. (2) cannot be directly used when precise irradiance measurements are required using a broad-band radiometer, such as in the irradiance profile observations using the aforementioned FVP. This condition can be attributed to the output voltage, which includes energy across a broader bandwidth range, and the corresponding irradiance, which represents an average value over this larger bandwidth range and cannot reflect the correct spectral irradiance. Thus, obtaining precise irradiance from broad-band data remains challenging.

This research shows that the key to obtaining accurate irradiance from broad-band data is to accurately understand the optical characteristics of the instrument and the signal, and then converting the voltage signal into accurate irradiance by correcting the output voltage signal across the broad bandwidth.

2.2 Bandwidth and transmissivity of an optical filter

The optical signal passing through the filter considerably differs from a rectangular signal, showing a peak-shaped structure, as illustrated in Fig. 2a.

Taking the 535 nm filter as an example, its transmissivity distribution is shown in Fig. 2b. The voltage $V_{\text{sd}}(\lambda_n)$ reflects the integral of the radiation energy entering the photodiode over the entire spectral range. The signal within the pink shaded area, which corresponds to the center wavelength ± 10 nm bandwidth, is required.

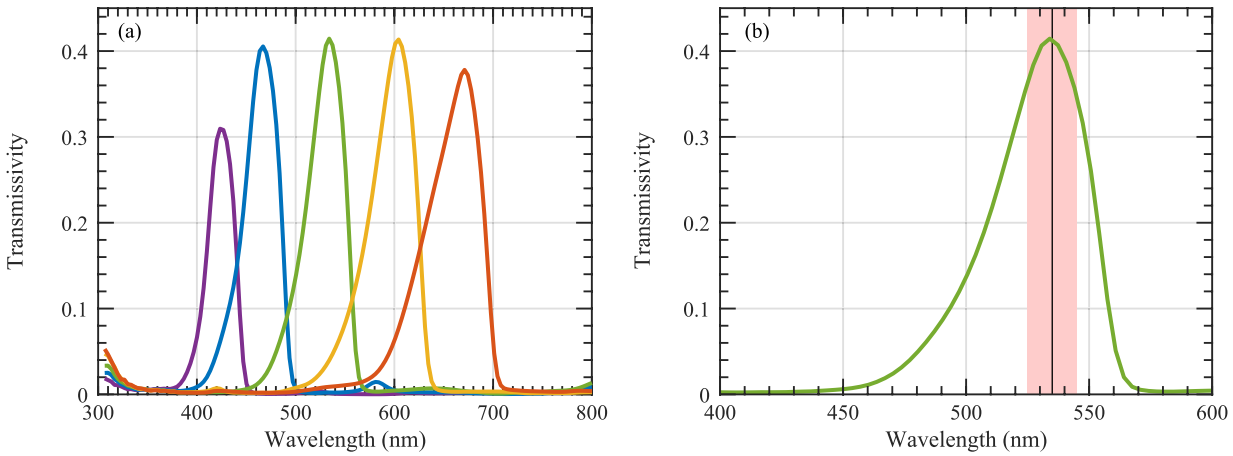

Fig. 2 **a** Measured transmissivity distribution of five filters of FVPs. **b** Transmissivity distribution of the 535 nm filter. The green solid line shows the transmissivity spectrum of the filter, the black solid line indicates the center wavelength, and the pink shading represents the bandwidth range

In Fig. 2b, some light outside the designated bandwidth can still pass through the filter and enter the photodiode. Therefore, precisely extracting the narrow-band voltages $v_{sd}(\lambda_n)$ and $v(\lambda_n)$ from the broad-band voltage $V_{sd}(\lambda_n)$ is necessary to apply Eqs. (2) and (3) for irradiance retrieval.

The spectral irradiance of the reference lamp is a known energy flux. Thus, the energy proportion within the designated ± 10 nm bandwidth range for each spectral band, $\sigma_{sd}(\lambda_n)$, can be calculated as follows:

$$\sigma_{sd}(\lambda_n) = \frac{1}{E_{max}} \frac{\int_{\lambda_n-\Delta\lambda}^{\lambda_n+\Delta\lambda} E_{sd}(\lambda)\gamma(\lambda)d\lambda}{\int_{\lambda_n-\Delta\lambda}^{\lambda_n+\Delta\lambda} \gamma(\lambda)d\lambda}, \tag{4}$$

where E_{max} is the maximum irradiance value of the reference lamp within the visible wavelength range. Equation (4) performs a weighted average of the radiation energy across each spectral band and normalizes the result. The weight coefficient $\gamma(\lambda)$ represents the transmissivity distribution with wavelength. Taking $\Delta\lambda = 10$ nm, the proportion $\sigma_{sd}(\lambda_n)$ for each spectral band is calculated.

As shown in Eq. (4), $\sigma_{sd}(\lambda_n)$ denotes the spectral characteristics of the reference lamp, that is, the variation of irradiance with wavelength, which is the average spectral value of the reference lamp within the specified bandwidth range. The actual transmissivity, $\gamma(\lambda_n)$, is considered to determine the amount of energy entering the photodiode. However, the actual transmissivities of each spectral band differ due to inevitable deviations in filter manufacturing. For example, the transmissivity at 427 nm is drastically lower compared to other spectral bands (Fig. 2a). Therefore, normalizing the transmissivity of each band is necessary.

$$\eta(\lambda_n) = \frac{\gamma(\lambda_n)}{\gamma_{max}}, \tag{5}$$

where γ_{max} is the maximum transmissivity of all spectral bands.

Correcting the broad-band voltage for bandwidth and transmissivity, the narrow-band voltage data are obtained as follows:

$$v_{sd}(\lambda_n) - v_{dark}(\lambda_n) = [V_{sd}(\lambda_n) - v_{dark}(\lambda_n)]\sigma_{sd}(\lambda_n)\eta(\lambda_n). \tag{6}$$

2.3 Determination of spectral transmissivity

According to Eq. (4), the spectral transmissivity $\gamma(\lambda)$ must be determined to accurately calculate $\sigma_{sd}(\lambda_n)$. Herein, a hyperspectral radiometer TriOS is used as the reference instrument. When the TriOS is positioned 50 cm from the reference lamp, the irradiance measured by TriOS is represented as $E_{\gamma 0}(\lambda)$. $E(\lambda)$ represents the irradiance measured by TriOS using an optical filter, a cosine collector, and a film at the same position. The overall spectral transmissivity of the three media is given by

$$\gamma(\lambda) = \frac{E(\lambda)}{E_{\gamma 0}(\lambda)} = \gamma_{film}(\lambda)\gamma_{cos}(\lambda)\gamma_{filt}(\lambda), \tag{7}$$

where $\gamma_{film}(\lambda)$, $\gamma_{cos}(\lambda)$, and $\gamma_{filt}(\lambda)$ are the transmissivities of the film, cosine collector, and filter, respectively. The $\gamma(\lambda)$ is the spectral response function, in which the response function of the photodiode is not included because it has not been used in the algorithm. Notably, measuring $E(\lambda)$ requires the close placement of the filter, cosine collector, and film against the TriOS lens

to maintain the measuring distance. And optical sealing is necessary. If a light-blocking lens is used and the measurement distance is altered, then the algorithms for obtaining $\gamma(\lambda)$ become remarkably complex.

As shown in Fig. 2a, each filter does not produce an ideal rectangular transmissivity but demonstrates a peaked transmissivity centered on the central spectrum, with an asymmetrically decreasing slope on either side. Therefore, regardless of the nominal spectral bandwidth of the filter, correcting voltage data to obtain accurate irradiance is necessary.

2.4 Determination of calibration coefficient

Substituting Eq. (6) into Eq. (3), the following is obtained:

$$S(\lambda_n) = \frac{\eta(\lambda_n)\sigma_{\mathrm{sd}}(\lambda_n)[V_{\mathrm{sd}}(\lambda_n) - v_{\mathrm{dark}}(\lambda_n)]}{E_{\mathrm{sd}}(\lambda_n)}. \tag{8}$$

Equation (8) indicates that an accurate irradiance can be derived from the energy within the narrow bandwidth obtained by adjusting the calibration coefficient. The two-point calibration was not tried in this study, because the calibration method we used follows the instructions of the National Institute of Metrology, China, and ensures sufficient accuracy. However, the two-point calibration method will be explored in the future to further improve the results.

Actual results show that Eq. (8) works well only when the light is nearly vertically incident. However, deviations will occur, occasionally significant, when the light is obliquely incident.

2.5 Influence of the film on transmittance

The upper surface of the instrument is covered with a film. This film alters the light energy entering the instrument, which can cause signal issues. Research has shown that the film changes the solar radiation flux entering the instrument, leading to measurement deviations under oblique incident light. This issue could be avoided by not using the film, but the current study still used the film because it is low-cost and can be used to secure the cosine collector. Additionally, the film can make the optical acquisition system waterproof.

The film is an optical medium that can affect incident light in three ways: (a) attenuation of the transmitted light, (b) spectral shift of the incident light, and (c) modification of the transmissivity for oblique incident light. Equation (7) encompasses the effect of the film on transmissivity. An air layer exists between the film and the cosine collector; thus, the impact on the spectral shift can be ignored. The focus should be on addressing the effect of the film on the transmissivity of oblique incident light.

Polarization occurs during the reflection and refraction of light at the film interface. According to optical polarization theory, the transmissivity considering polarization is a function related to the wavelength (Akhmanov and Nikitin 1997):

$$T(\lambda_n) = 1 - \frac{1}{2}\left[\frac{\tan^2(i_1 - i_2)}{\tan^2(i_1 + i_2)} + \frac{\sin^2(i_1 - i_2)}{\sin^2(i_1 + i_2)}\right], \tag{9}$$

where i_1 and i_2 are the incidence and refraction angles, respectively, as determined by Snell's law (Shirley 1951):

$$n_1 \sin i_1 = n_2 \sin i_2, \tag{10}$$

where n_1 and n_2 are the refractive indices of the atmosphere and the film, respectively. The nominal refractive index of the film is the refractive index of yellow sodium light (Rao 1997). For oblique incidence, the refractive indices of light at various incident angles are different, facilitating dispersion (Louisnathan et al. 1978). The relationship between refractive index and wavelength is as follows (Mu and Li 1965):

$$\frac{n_1}{n_2} = \frac{\lambda_2}{\lambda_1}. \tag{11}$$

Assuming that the wavelength λ_0 of yellow sodium light is 589.3 nm and the nominal refractive index n_0 of the film is 1.73, then

$$n' = \frac{n_0\lambda_0}{\lambda}. \tag{12}$$

That is, the refractive index *n'* is inversely proportional to the wavelength. The results obtained using Eq. (12) are shown in Table 1. The table reveals that the actual refractive indices of short waves are higher than the nominal refractive index, while the actual refractive indices of long waves are lower.

The transmissivity calculated using Eq. (9) is shown by the black curve in Fig. 3. Notably, the transmissivity remains relatively stable when the incident angle is within 40°, but decreases substantially when the incident angle is greater than 40°. When the incident angle exceeds the Brewster angle (approximately equal to 62.2°), the transmissivity decreases sharply. This is the reason for the significant errors of retrieved irradiance at oblique incidence.

Table 1 Relationship between the transmissivity and refractive index of the film

Parameter	Wavelength (nm)				
	427	474	535	606	671
Refractive index	2.366	2.131	1.888	1.667	1.505
Transmissivity	0.825	0.858	0.892	0.925	0.948

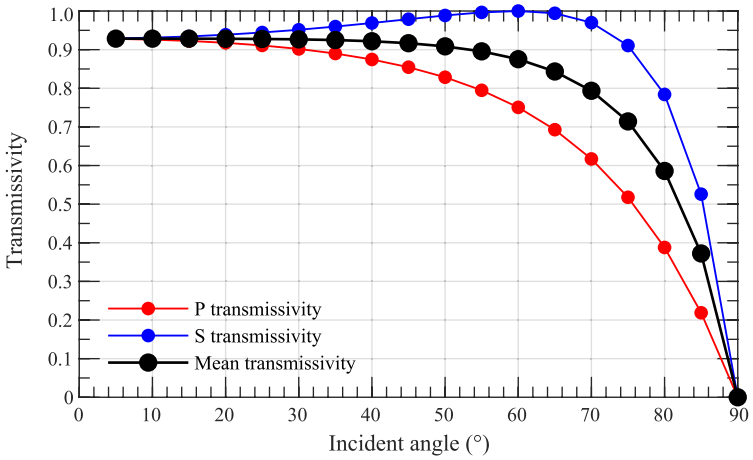

Fig. 3 Variation of transmissivity of the film with incident angle (solar zenith angle). The P transmissivity (red curve) represents the transmissivity due to the electric vector parallel to the plane of incidence, while the S transmissivity (blue curve) represents the transmissivity due to the electric vector perpendicular to the plane of incidence. The mean transmissivity (black curve) is the average value of the P transmissivity and the S transmissivity (Born and Wolf 1999)

The difference in refractive index caused by polarization results in differences in transmissivity. For example, with light incident at an angle of 46°, the transmissivity is highest and lowest for long and short wavelengths, respectively. Under oblique incidence conditions, the film attenuates the transmitted light, resulting in less energy being received by the photodiode. Dividing the irradiance by the transmissivity is necessary to eliminate the optical effect of the film. Transmissivity, an environmental parameter, depends on the incident angle; thus, it cannot be included in the calibration coefficients and must only be corrected sample by sample. That is,

$$E(\lambda_n) = \frac{v(\lambda_n) - v_{\text{dark}}(\lambda_n)}{S(\lambda_n)T(\lambda_n)}. \tag{13}$$

The physical meaning of this correction is as follows: when light is incident at an oblique angle, the photodiode receives light signals that are additionally attenuated by the film, leading to a retrieved irradiance that is lower than the actual value. The transmissivity $T(\lambda_n)$ represents the proportion of the additional attenuated light signal. Therefore, the accurate retrieved irradiance can be obtained by correcting the corresponding voltage signal.

However, Eq. (13) has limitations: this equation is highly accurate when the solar zenith angle is small, but the error increases rapidly as the solar zenith angle approaches 90°. This study analyzed the cause of this issue as follows: the transmissivity given by Eq. (13) is applicable only to direct light. Under conditions of heavy fog, the instrument still receives scattered light from the fog, even in the absence of direct light. Therefore, considering direct and scattered light is necessary in the retrieval algorithm.

Assume that $T(\lambda_n)$ comprises two parts:

$$\kappa(\lambda_n) = T_{\max}(\lambda_n)\left\{[1 - f(\lambda_n)] + f(\lambda_n)\frac{T(\lambda_n)}{T_{\max}(\lambda_n)}\right\}, \tag{14}$$

where $T_{\max}(\lambda_n)$ is the maximum value of transmissivity, and $f(\lambda_n)$ represents the effect of direct light on irradiance. When the zenith angle is at its minimum, the transmissivity is at its maximum, and $\kappa(\lambda_n)$ is equal to the maximum transmissivity $T_{\max}(\lambda_n)$, resulting in a good correction effect. When the zenith angle is at its maximum, the transmissivity is remarkably low, and $\kappa(\lambda_n)$ corresponds to the effect of scattered light, approaching $[1-f(\lambda_n)]T_{\max}(\lambda_n)$.

The proportion of scattered to direct light is constantly changing, and applicable theories or established experiences for directly determining $f(\lambda_n)$ are unavailable. In practice, this proportion can only be determined empirically by performing a retrieval algorithm on all comparative measurement data and selecting $f(\lambda_n)$ that yields the smallest relative deviation between the retrieved and actual irradiance as the calibration coefficient. Figure 4 shows the statistical results based on data from 34 valid in situ observation profiles at Qianliyan Ocean Station. FVPs and a TriOS were used to measure downward irradiance during the observation. As presented in Fig. 4, the mean relative deviation is minimized when $f(\lambda_n)$ is set to 0.4. The physical significance of $f(\lambda_n)$ expressed by Eq. (14) is that, despite the constantly changing proportion of direct and scattered light, a ratio can still

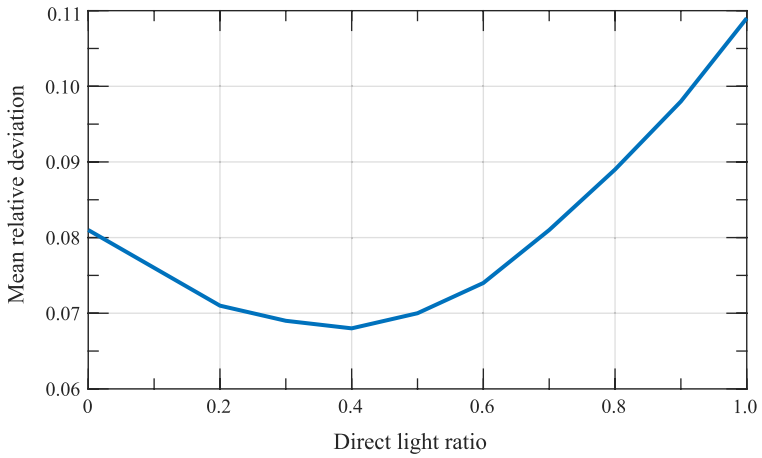

Fig. 4 Relationship between the mean relative deviation of the retrieved irradiance and the proportion of direct light based on the data from 34 valid in situ observation profiles at Qianliyan Ocean Station

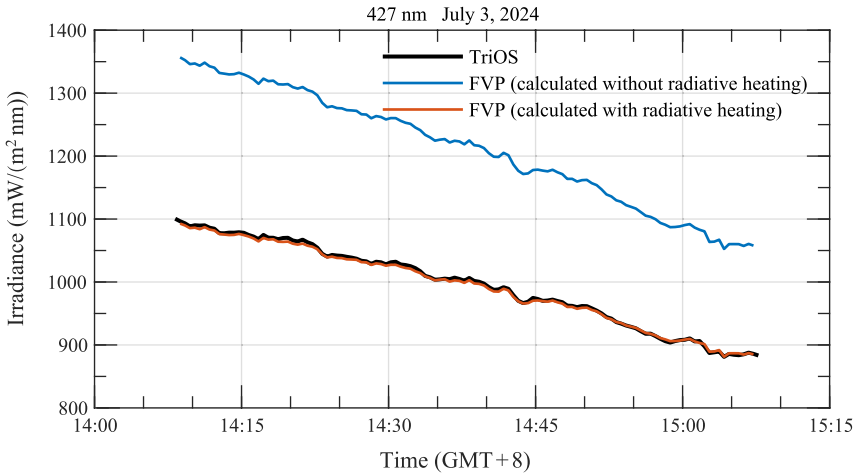

Fig. 5 Errors in retrieved irradiance under strong radiation conditions. This data is from the Baguan Mountain validation test in Qingdao on July 3, 2024. The irradiance of FVP (blue line) significantly deviated from the reference radiometer data (black line), but it was remarkably improved by the radiative heating correction (red line)

be determined for the entire observation process to achieve the minimum relative deviation of the retrieved irradiance.

Therefore, when the solar zenith angle during observation is known, Eq. (13) is adjusted to

$$E(\lambda_n) = \frac{\nu(\lambda_n) - \nu_{\text{dark}}(\lambda_n)}{S(\lambda_n)\kappa(\lambda_n)}. \tag{15}$$

This result indicates that for data obtained using a broad-band filter, the standard calibration process can only accurately retrieve the irradiance of vertically incident sunlight. When the sunlight is incident at an angle, additional correction is required to eliminate the polarization effects caused by the film.

2.6 Errors under strong radiation conditions

The corrected data aligns well with the results from TriOS. However, the error remains substantial under strong radiation conditions (the blue curve in Fig. 5). These deviations are attributed to solar radiative heating. Solar radiation affects the instrument in two ways: first, solar radiation heats the plastic housing and increases its temperature, which generates additional thermal radiation that affects the energy received by the photodiode; second, solar radiation increases the temperature of the photodiode circuit, which may alter the dark current and, in turn, change the calibration coefficient of the radiometer. Both effects are caused by radiative heating under strong solar radiation conditions. Therefore, an extra

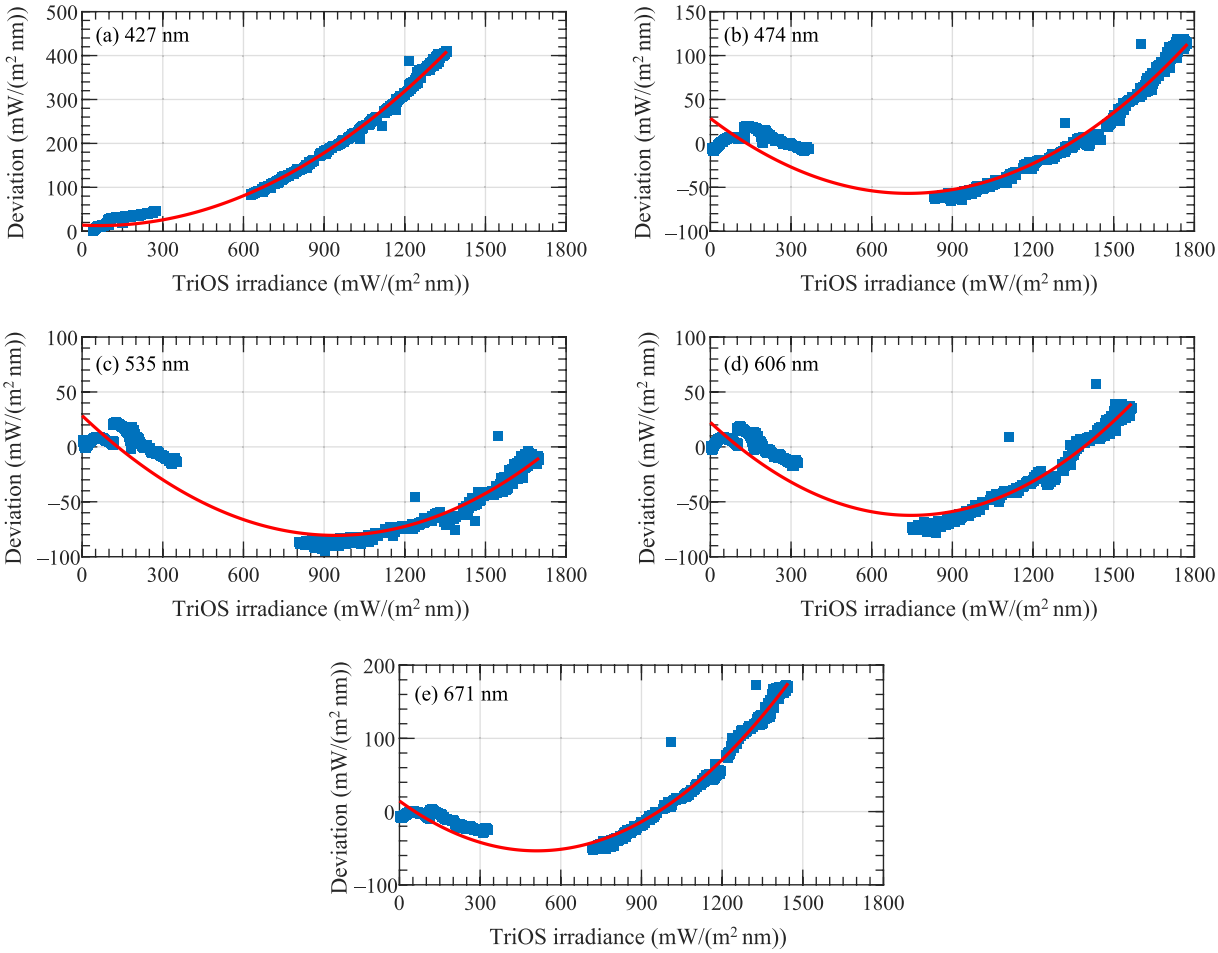

Fig. 6 Relationship between the deviation of the retrieved irradiance for each wave band of FVP and the actual irradiance (measured by TriOS) for sunny weather conditions from the Baguan Mountain validation test in Qingdao on July 3, 2024. Red lines are fitted curves

correction for radiative heating should be developed to further correct the irradiance measurement result.

Figure 6 shows the varying deviations of the retrieved irradiance with the actual irradiance under sunny weather conditions. Notably, the deviation is closely related to actual irradiance under the condition of strong sunlight. The result indicates that the error caused by radiative heating can be corrected by its relationship with actual irradiance.

Suppose the measured spectral irradiance affected by radiative heating is $E_0(\lambda_n)$, and the irradiance deviation caused by radiative heating is $\Delta E_0(\lambda_n)$. Thus, the irradiance due to solar radiation only is $E(\lambda_n)$:

$$E(\lambda_n) = E_0(\lambda_n) - \Delta E_0(\lambda_n). \tag{16}$$

Based on the deviation curve of $\Delta E_0(\lambda_n)$ with $E_{\text{trios}}(\lambda_n)$ (Fig. 6), they can be fitted quadratically as

$$\Delta E_0(\lambda_n) = a(\lambda_n) + b(\lambda_n)E_{\text{trios}}(\lambda_n) + c(\lambda_n)E^2_{\text{trios}}(\lambda_n), \tag{17}$$

where $E_{\text{trios}}(\lambda_n)$ is the irradiance measured by TriOS. The response to radiative heating varies for each spectral band; therefore, $a(\lambda_n)$, $b(\lambda_n)$, and $c(\lambda_n)$ are related to the spectral bands and must be fitted from the measured data $E_{\text{trios}}(\lambda_n)$. The fitted result is illustrated by the red line in Fig. 6, which represents the deviation caused by radiative heating.

Replacing $E_{\text{trios}}(\lambda_n)$ in Eq. (17) with $E(\lambda_n)$, and then substituting the equation into Eq. (16), the following is obtained:

$$E(\lambda_n) = E_0(\lambda_n) - \Big[a(\lambda_n) + b(\lambda_n)E(\lambda_n) + c(\lambda_n)E^2(\lambda_n)\Big], \tag{18}$$

solving Eq. (18) yields:

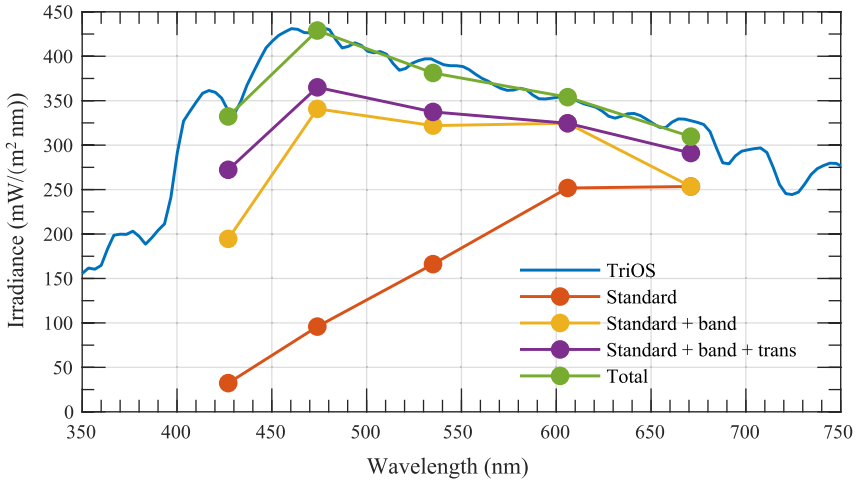

Fig. 7 Results of different correction methods. This data is from the 34th sea fog profile observed at the Qianliyan Ocean Station on April 28, 2024

$$E(\lambda_n) = \frac{-[1 + b(\lambda_n)] + \sqrt{[1 + b(\lambda_n)]^2 - 4c(\lambda_n)[a(\lambda_n) - E_0(\lambda_n)]}}{2c(\lambda_n)}. \tag{19}$$

Equation (19) is the final corrected result, which effectively eliminates the impact of radiative heating (the red line in Fig. 5).

2.7 Roles of various corrections

This study presents various correction algorithms to address the low accuracy of irradiance retrieval from data measured by broad-band radiometers. For example, during the 34th sea fog profile observation at the Qianliyan Ocean Station, FVPs and TriOS were used simultaneously. The results of the correction methods are shown in Fig. 7. The observation was performed at 8:01 am on April 28, 2024, with a solar zenith angle of 57.35°. The presence of dense fog during the observation increased the representativeness of the correction.

In Fig. 7, the curve labeled 'Standard' denotes the correction results obtained in accordance with the standard calibration of Eq. (3). This curve indicates a substantial difference between the broad-band data and the results from the reference radiometer, with the deviation increasing as the wavelength decreases. The curve labeled 'Standard + band' represents the results after applying the bandwidth correction $\sigma_{sd}(\lambda_n)$, which converts the broad-band data into narrow-band data, notably improving the results. However, a substantial error remains in the short-wave region. The curve labeled 'Standard + band + trans' includes the correction of transmissivity, as shown in Eq. (8), drastically improving the transmissivity in spectral bands with originally low transmissivity. The curve labeled 'Total' represents 'Standard + band + trans + film', adding the correction for film, reflecting the additional effect of polarization on transmissivity. The observation time shown in Fig. 7 is 8:00 am, and the solar radiation was relatively weak; thus, corrections in radiative heating are no longer necessary.

After applying these corrections, the retrieved irradiance closely matches the measurements from the reference radiometer, indicating the reliability of the correction algorithms.

3 Validation of the bandwidth correction algorithm

The algorithm in this paper cannot be tested in the laboratory. Thus, validation tests in the field are necessary to demonstrate its reliability. Under varying weather conditions and different solar zenith angles, the FVP and reference radiometer (TriOS) should be jointly used for synchronized observations to determine the accuracy of retrieved irradiance.

The validation tests were conducted from July 3–5, 2024, at the Baguan Mountain Meteorological Observatory of the Ocean University of China. The weather was clear on July 3 and cloudy on the other days. The daily experiments ran from noon to 6:00 pm to test the adaptability of the algorithm to different solar zenith angles, providing measurement results that satisfy the minimum and maximum zenith angles. The observation time limitation for the FVP instrument is within one hour; thus, the instrument must be restarted after each observation. Therefore, more than five comparative observations per day were conducted, with a 10 min interruption between each observation. A hyperspectral radiometer TriOS was used as a reference radiometer.

The fitting coefficients $a(\lambda_n)$, $b(\lambda_n)$, and $c(\lambda_n)$ were determined using the data observed on July 3 (Fig. 6) and

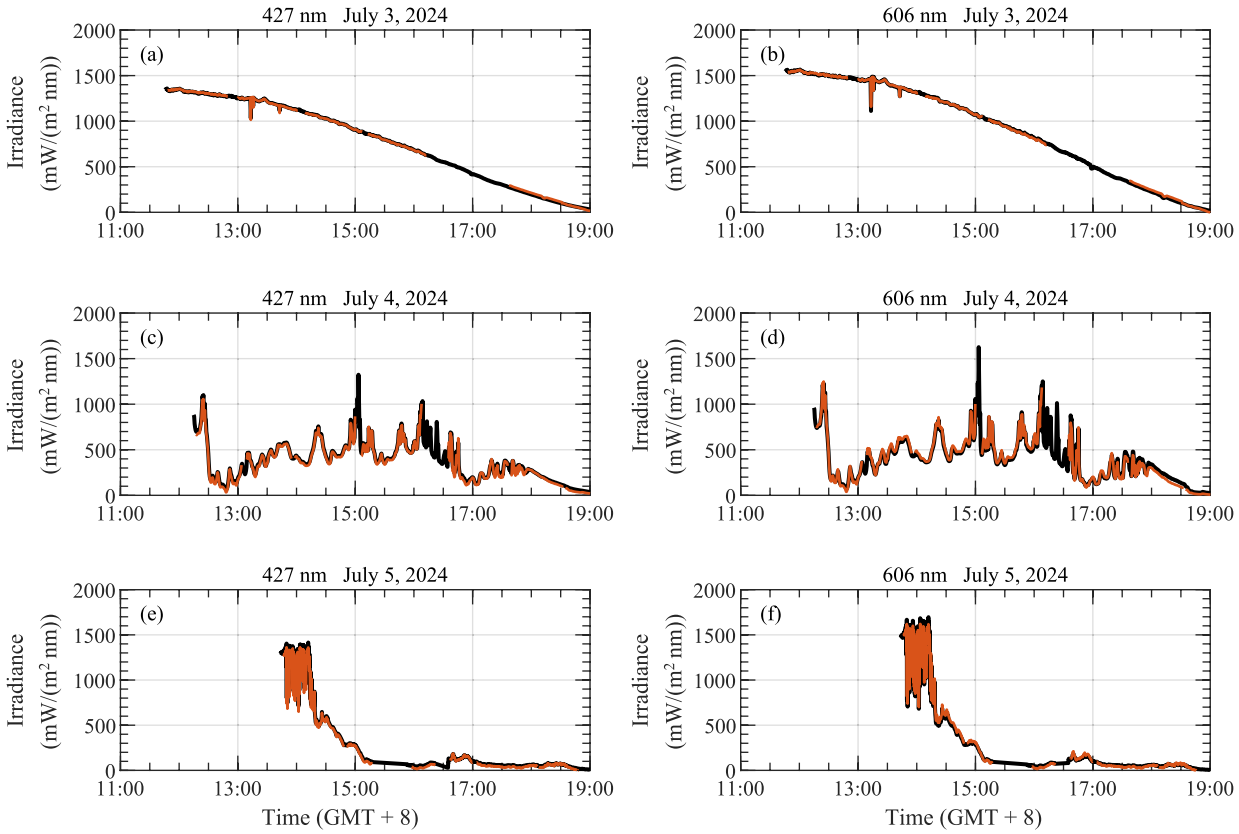

Fig. 8 Time series of irradiance at 427 and 606 nm from FVP (red line) and the reference radiometer TriOS (black line) in the Baguan Mountain validation test in Qingdao

were used for calibration of all FVP data. The results for 427 and 606 nm are shown in Fig. 8, with similar results obtained for other spectral bands that are not presented in this paper. In Fig. 8, the retrieved irradiance is highly consistent with the irradiance from the TriOS, both in the overall trend and in the details of changes caused by clouds. This result demonstrates that the SIBOF algorithm meets the accuracy requirements for data correction.

Figure 9 shows the comparison between the data from FVP and TriOS, indicating that the retrieved irradiance is highly consistent with the irradiance measured by TriOS, regardless of whether the radiation is strong or weak.

Table 2 shows the relative deviations of the retrieved irradiance for each day and each spectral band obtained in the validation test. The fitting coefficients $a(\lambda_n)$, $b(\lambda_n)$, and $c(\lambda_n)$ were obtained from the data on July 3, 2024, with the relative deviations of the retrieved irradiance for this day being below 2%. The relative deviations of most spectral bands for other days are below 7%, with only the 671 nm band being below 11%, indicating that the results achieved high accuracy and satisfied the product standards of FVP (below 15%).

4 Applications of the SIBOF algorithm

In April 2024, a 20-day sea fog observation was conducted at Qianliyan Ocean Station, where a total of 38 FVPs were launched. Three profiles under thick fog, along with several profiles without fog, were observed, and ground observations were conducted with TriOS simultaneously. The irradiance obtained from FVPs was corrected with the SIBOF algorithm, and the corrected irradiance obtained before the balloons were released can be compared with the observations from TriOS.

Under field conditions, the results cannot be verified with the true values of irradiance, and only comparative measurements can be conducted. Field experiments differ from standardized tests and inherently have some uncertain factors: (1) the observation positions of TriOS and FVPs are inconsistent due to the complex terrain and sunlight conditions on the island, affecting their comparability. (2) A notable spatial difference in irradiance during thick fog is observed. Thus, any deviation may represent the actual situation at different positions and may not necessarily indicate an issue with the correction algorithm. (3) During measurements, TriOS was placed

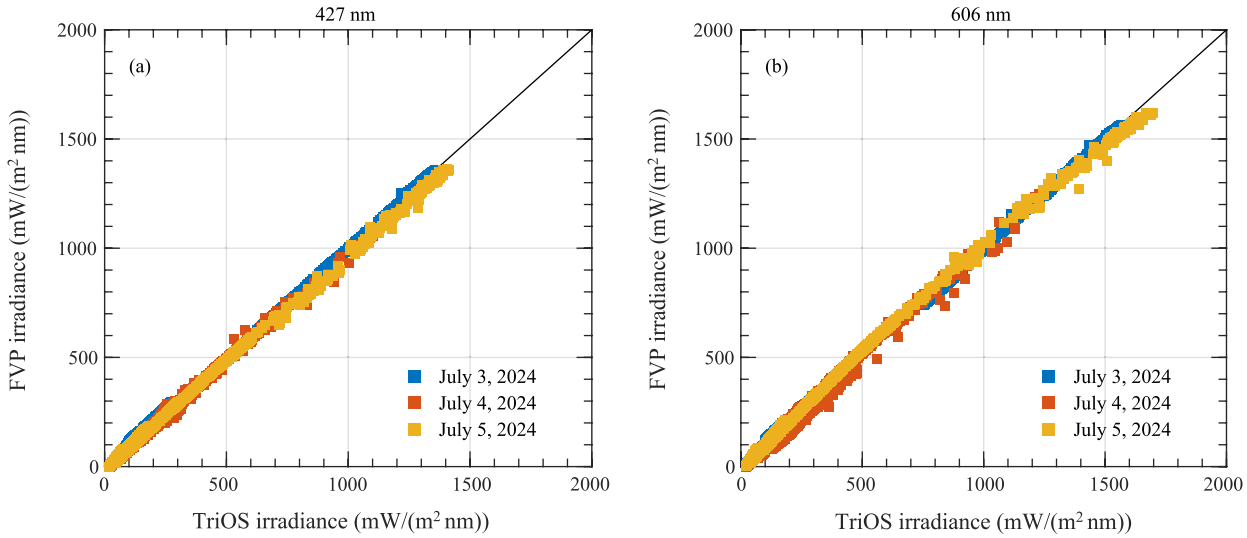

Fig. 9 Relationship between the synchronous observation results of the FVP and the reference radiometer TriOS in the validation test at Baguan Mountain, Qingdao

Table 2 Relative deviations of the retrieved irradiance for each day and each spectral band obtained in the validation test at Baguan Mountain, Qingdao (unit: %)

Date	Wavelength (nm)				
	427	474	535	606	671
July 3, 2024	1.58	1.93	1.82	1.72	1.47
July 4, 2024	4.66	4.73	5.42	6.55	10.41
July 5, 2024	3.34	3.75	2.82	5.37	10.68

in an unobstructed location, while the FVPs had a sounding balloon attached above, which may have influenced the reception of the direct light.

A total of 38 data sets were obtained during Qianliyan observation, of which five profiles (Profiles 2, 11, 29, 30, and 35) must be excluded due to the rain or substantial spatial difference in irradiance in thick fog. The relative deviations of the remaining FVP corrected data are shown in Fig. 10. Notably, the average relative deviations of all profiles are below 15%, with 28 profiles having an average relative deviation below 10%. The results indicate that the SIBOF algorithm meets the practical requirements.

The comparison of retrieved irradiance from FVP with synchronous observed irradiance from TriOS is shown in Fig. 11. Notably, in foggy conditions, the irradiance is generally below 800 mW/(m^2 nm), and all values are close to the diagonal line, indicating that the SIBOF algorithm can provide accurate retrieved results. In conditions of higher irradiance, which corresponds to fog-free weather conditions with dominant direct light, the retrieved results for Profiles 37 and 19 visually show a larger deviation. However, the relative deviation for both profiles is below 15%, which meets the product standard requirements.

5 Results and conclusions

A disposable miniature radiometer that uses optical filters for spectral separation, also known as the FVP, has been developed. This study aimed to achieve precise irradiance measurements in profile observations. However, the obtained data include out-of-band signals due to the broad bandwidth of the filters and their peak-shaped transmissivity structures, leading to remarkable errors. This paper proposes a SIBOF algorithm that achieves accurate retrieved irradiance through four correction steps.

The first step is called energy ratio correction. Initially, the broad-band data are corrected using energy ratio $\sigma_{\mathrm{sd}}(\lambda_n)$. The physical meaning of $\sigma_{\mathrm{sd}}(\lambda_n)$ is the proportion of light energy received within the bandwidth $\pm\Delta\lambda$. Through this coefficient, the data of broad bands are converted into those of narrow bands. Another crucial role of $\sigma_{\mathrm{sd}}(\lambda_n)$ is to eliminate the considerable differences between the reference lamp and solar spectra, increasing the applicability of the calibration coefficients obtained from the reference lamp to the solar spectrum. $\sigma_{\mathrm{sd}}(\lambda_n)$ reflects the interaction between the reference lamp spectrum and the filter transmissivity, defining the measurement system constituted by incident light and the filter. The applicability of this relationship under various natural light conditions has been proven, disregarding the differences in illumination conditions between foggy and non-foggy situations.

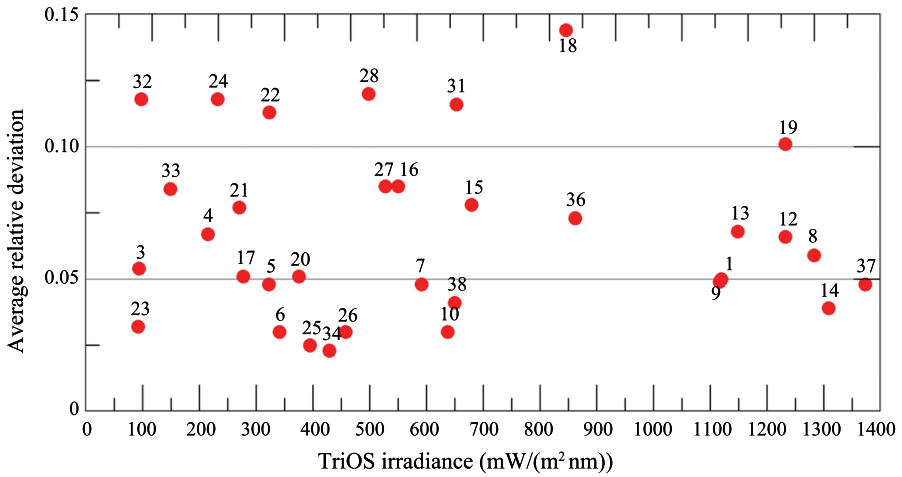

Fig. 10 Average relative deviations between the retrieved irradiance of FVPs and the synchronous observed irradiance from TriOS across different profiles of the sea fog observation at Qianliyan Ocean Station. The numbers in the figure represent the profile numbers

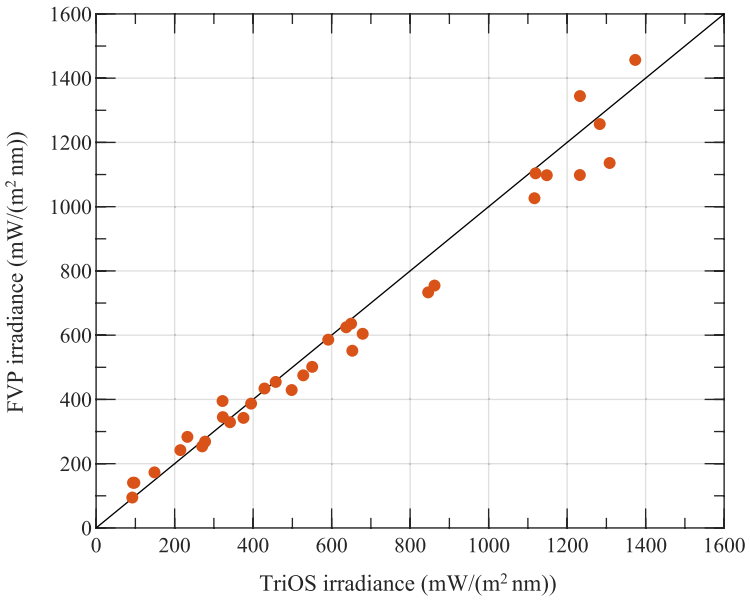

Fig. 11 Comparison of the retrieved irradiance from FVPs with the synchronous observed irradiance from TriOS. This data is from the sea fog observation at the Qianliyan Ocean Station

The second step is called transmissivity correction. The differences in filter transmissivity $\gamma(\lambda_n)$ are mainly due to the control process of coating thickness during production. The coating materials differ across wavelengths; thus, achieving the same transmissivity for filters at different wavelengths is difficult. Therefore, $\gamma(\lambda_n)$ is normalized and multiplied by the calibration coefficient, which effectively corrects the impact caused by differences in filter transmissivity, making the measurement results of each spectral band comparable.

The third step is called polarization correction. The film overlying on the cosine collector acts as a polarizer on the transmitted light, generating polarized light. When the incident angle is large, the transmissivity of light through the film changes, causing substantial errors that require additional correction to obtain accurate irradiance. This paper proposes obtaining the polarization-induced transmissivity based on the refractive index and transmissivity of the film in each spectral band and incorporating it into the correction algorithm to eliminate errors induced by the polarization effect of the film.

The fourth step is called radiative heating correction. Solar radiation can affect the instrument in two ways.

First, solar radiation involves heating the plastic housing and increasing its temperature, which generates additional thermal radiation that affects the energy received by the photodiode. Second, solar radiation increases the temperature of the photodiode circuit, which may alter the dark current and, in turn, change the calibration coefficient of the radiometer. Therefore, a fitting curve for the irradiance deviation is derived as a function of actual irradiance, and the data are corrected accordingly. The results show that the four-step correction method achieves highly accurate irradiance data.

From July 3–5, 2024, standardized tests were conducted at Baguan Mountain Meteorological Observatory in Qingdao to validate the effectiveness of the above algorithms. The results indicate that, whether under cloudy or clear weather conditions, the retrieved irradiance closely matches the data from the reference radiometer. Thus, the algorithm yields ideal measurement results and proves to be a reliable correction algorithm.

In April 2024, a sea fog observation was conducted using FVPs and a TriOS at Qianliyan Ocean Station, where 38 FVPs with sounding balloons were launched, and simultaneous ground observations using a hyperspectral radiometer TriOS as reference radiometer were conducted for comparison. Before the balloons were launched, the data obtained from FVPs could be compared with those from TriOS to conduct an application experiment on the SIBOF algorithm. The results showed that the irradiance obtained using the SIBOF algorithm had good consistency with the reference radiometer.

Therefore, this study demonstrates that the data obtained using optical filters with broad bands have substantial deviations. The SIBOF algorithm presented in this paper can effectively correct the broad-band data and achieve accurate retrieved irradiance.

Acknowledgements
This work is supported by the National Key R&D Program of China (Grant No 2019YFA0607000) and the National Natural Science Foundation of China (Grant Nos. 42106221, 41941012, 42475099). Thanks to Prof. Tinglu Zhang and Prof. Shuguo Chen for their support and assistance in atmospheric optics theory and technology. We would like to thank the Disaster Reduction Forecasting Center of the Beihai Bureau of the Ministry of Natural Resources and the Qianliyan Ocean Station for their support in the field observation of sea fog.

Additional information
Edited by: Lin Gao.

Authors' contributions
Yilin Liu: Conceptualization, Methodology, Data Curation, Software, Validation, Writing-Original Draft; Jinping Zhao: Conceptualization, Methodology, Formal Analysis, Resources, Supervision, Software, Writing-Original Draft; Ping Chen: Conceptualization, Methodology, Data Curation, Writing-Original Draft; Xianyao Chen: Conceptualization, Formal Analysis, Supervision; Li Yi: Resources, Data Curation; Xiaoyu Wang: Validation, Data Curation; Tao Li: Methodology, Data Curation.

Availability of data and materials
The data and references presented in this study are available from the corresponding author upon reasonable request.

Declarations

Ethics approval and consent to participate
Not applicable.

Consent for publication
Not applicable.

Competing interests
The authors declare that they have no competing interests, and the manuscript is approved by all authors for publication.

Received: 13 August 2024 Revised: 3 September 2024 Accepted: 13 September 2024
Published online: 08 October 2024

References

Akhmanov SA, Nikitin SY (1997) Physical optics. Oxford University Press, New York
Bird RE, Riordan C (1986) Simple solar spectral model for direct and diffuse irradiance on horizontal and tilted planes at the Earth's surface for cloudless atmospheres. J Appl Meteorol Climatol 25(1):87–97. https://doi.org/10.1175/1520-0450(1986)025%3c0087:SSSMFD%3e2.0.CO;2
Born M, Wolf E (1999) Principles of optics: electromagnetic theory of propagation, interference and diffraction of light. Cambridge University Press, Cambridge
Bruegge CJ, Stiegman AE, Rainen RA, Springsteen AW (1993) Use of Spectralon as a diffuse reflectance standard for in-flight calibration of Earth-orbiting sensors. Opt Eng 32(4):805–814. https://doi.org/10.1117/12.132373
Du BW (2023) Research on key techniques of multi-beam interference micro spectrometer. PhD thesis, University of Chinese Academy of Sciences
Dunkelman L, Scolnik R (1959) Solar spectral irradiance and vertical atmospheric attenuation in the visible and ultraviolet. J Opt Soc Am 49(4):356–367. https://doi.org/10.1364/JOSA.49.000356
Eltbaakh YA, Ruslan MH, Alghoul MA, Othman MY, Sopian K, Razykov TM (2012) Solar attenuation by aerosols: an overview. Renew Sust Energy Rev 16(6):4264–4276. https://doi.org/10.1016/j.rser.2012.03.053
Epstein LI (1952) The design of optical filters. J Opt Soc Am 42(11):806–810. https://doi.org/10.1364/JOSA.42.000806
Ermolli I, Matthes K, Dudok de Wit T, Krivova NA, Tourpali K, Weber M et al (2013) Recent variability of the solar spectral irradiance and its impact on climate modelling. Atmos Chem Phys 13(8):3945–3977. https://doi.org/10.5194/acp-13-3945-2013
Fan BX, Nie YX, Yang GZ (2009) Encyclopedia of China · Physics (2nd ed). Encyclopedia of China Publishing House, Beijing (in Chinese)
Girish BS, Srivani KS, Subrahmanyan R, Udaya Shankar N, Singh S, Jishnu Nambissan T et al (2020) SARAS CD/EoR radiometer: design and performance of the digital correlation spectrometer. J Astron Instrum 9(2):2050006. https://doi.org/10.1142/S2251171720500063
Gray LJ, Beer J, Geller M, Haigh JD, Lockwood M, Matthes K et al (2010) Solar influences on climate. Rev Geophys 48(4):RG4001. https://doi.org/10.1029/2009RG000282
Hahn DW (2009) Light scattering theory. University of Florida, Gainesville
Khalil SA, Shaffie AM (2016) Attenuation of the solar energy by aerosol particles: a review and case study. Renew Sust Energy Rev 54:363–375. https://doi.org/10.1016/j.rser.2015.09.085
Kleinman RE, Senior TBA (1986) Rayleigh scattering. In: Mechanics and mathematical methods–series of handbooks, vol 2. Elsevier, Amsterdam, pp 1–70
Li JF, Lin GY, Wu H, Duan MZ, Cao DS, Wang LQ (2022) Design and verification of a double-grating spectrometer system (DGSS) for simultaneous observation of aerosols, water vapor and clouds. Remote Sens 14(10):2492. https://doi.org/10.3390/rs14102492
Louisnathan SJ, Bloss FD, Korda EJ (1978) Measurement of refractive indices and their dispersion. Am Miner 63(3–4):394–400
Luo HY, Shi HL, Li ZW, Li S, Xiong W, Hong J (2016) Study on the spectral characteristics of narrow-band filter in SHS. Spectrosc Spectr Anal 35(4):1116–1119 (in Chinese with English abstract)

Ma L (2007) Measurement of aerosol size distribution function using Mie scattering–mathematical considerations. J Aerosol Sci 38(11):1150–1162. https://doi.org/10.1016/j.jaerosci.2007.08.003
McCartney EJ (1976) Optics of the atmosphere: scattering by molecules and particles. Wiley, Chichester
Meftah M, Bolsée D, Damé L, Hauchecorne A, Pereira N, Irbah A et al (2016) Solar irradiance from 165 to 400 nm in 2008 and UV variations in three spectral bands during solar cycle 24. Sol Phys 291:3527–3547. https://doi.org/10.1007/s11207-016-0997-8
Mercado LM, Bellouin N, Sitch S, Boucher O, Huntingford C, Wild M et al (2009) Impact of changes in diffuse radiation on the global land carbon sink. Nature 458(7241):1014–1017. https://doi.org/10.1038/nature07949
Michael PR, Johnston DE, Moreno W (2020) A conversion guide: solar irradiance and lux illuminance. J Meas Eng 8(4):153–166. https://doi.org/10.21595/jme.2020.21667
Mu GG, Li RY (1965) General physics: optical part. Higher Education Press, Beijing (in Chinese)
Mueller H (1938) On the theory of scattering of light. Proc R Soc London A 166(926):425–449. https://doi.org/10.1098/rspa.1938.0102
Mueller JL, Fargion GS (2003) Ocean optics protocols for satellite ocean color sensor validation, revision 4, volume III: radiometric measurements and data analysis protocols. In: Technical report. NASA, Goddard Space Flight Space Center, Maryland, pp 1–63. https://doi.org/10.25607/OBP-62
Murgai V, Klein S, Arnold W, Durell C, Bowers S, Russell B et al (2020) Low degradation Spectralon selection. In: Earth Observing Systems XXV. SPIE, pp 171–180. https://doi.org/10.1117/12.2568774
Okhonin S, Gureev M, Sallin D, Appel J, Koukab A, Kvasov A et al (2015) A dynamic operation of a PIN photodiode. Appl Phys Lett 106(3):031115. https://doi.org/10.1063/1.4906488
Pagano TS, Johnson DL, McGuire JP, Schwochert MA, Ting DZ (2022) Technology maturation efforts for the next generation of grating spectrometer hyperspectral infrared sounders. IEEE J Sel Top Appl Earth Observ Remote Sens 15:2929–2943. https://doi.org/10.1109/JSTARS.2022.3165168
Rao SM (1997) Spectrographic technique for determining refractive indices. Opt Eng 36(1):162–166. https://doi.org/10.1117/1.601127
Richard E, Harber D, Coddington O, Drake G, Rutkowski J, Triplett M et al (2020) SI-traceable spectral irradiance radiometric characterization and absolute calibration of the TSIS-1 spectral irradiance monitor (SIM). Remote Sens 12(11):1818. https://doi.org/10.3390/rs12111818
Riihimaki LD, Flynn C, McComiskey A, Lubin D, Blanchard Y, Chiu JC et al (2021) The shortwave spectral radiometer for atmospheric science: capabilities and applications from the ARM user facility. Bull Am Meteorol Soc 102(3):E539–E554. https://doi.org/10.1175/BAMS-D-19-0227.1
Shirley JW (1951) An early experimental determination of Snell's law. Am J Phys 19(9):507–508. https://doi.org/10.1119/1.1933068
Sun CL, Chen ZQ, Yin YX, Ye YT, Luo Y, Ma H et al (2022) Broadband and high-resolution integrated spectrometer based on a tunable FSR-free optical filter array. ACS Photonics 9(9):2973–2980
Tatsiankou V, Hinzer K, Haysom J, Schriemer H, Emery K, Beal R (2016) Design principles and field performance of a solar spectral irradiance meter. Sol Energy 133:94–102. https://doi.org/10.1016/j.solener.2016.03.054
Thuillier G, Zhu P, Snow M, Zhang P, Ye X (2022) Characteristics of solar-irradiance spectra from measurements, modeling, and theoretical approach. Light-Sci Appl 11(1):1–5. https://doi.org/10.1038/s41377-022-00750-7
Wang WB (2014) Exploring the variation of solar spectral characteristic in atmosphere and ocean principal wavelength. PhD thesis, Ocean University of China
Wiscombe WJ (1980) Improved Mie scattering algorithms. Appl Opt 19(9):1505–1509
Yang ZY, Albrow-Owen T, Cai WW, Hasan T (2021) Miniaturization of optical spectrometers. Science 371(6528):eabe0722. https://doi.org/10.1126/science.abe0722
Young AT (1981) Rayleigh scattering. Appl Opt 20(4):533–535. https://doi.org/10.1364/AO.20.000533
Zhang L, Li JH, Li HS, Zhang PF, Zhou AM, Li B et al (2024a) A high resolution prism-grating panoramic imaging spectrometer based on occultation observations. Opt Commun 560:130436. https://doi.org/10.1016/j.optcom.2024.130436
Zhang YS, Wang K, Yue W, Liu SK, Yu JL, Ye X (2024b) Optical design and stray light analysis of underwater spectral radiometer. Appl Sci 14(8):3172. https://doi.org/10.3390/app14083172
Zimmer L, Domann R, Hardalupas Y, Ikeda Y (2003) Simultaneous laser-induced fluorescence and Mie scattering for droplet cluster measurements. AIAA J 41(11):2170–2178. https://doi.org/10.2514/2.6835

Publisher's Note